

Optical slicing of human retinal tissue *in vivo* with the adaptive optics scanning laser ophthalmoscope

Fernando Romero-Borja, Krishnakumar Venkateswaran, Austin Roorda, and Thomas Hebert

We present imaging results in human retinal tissue *in vivo* that allowed us to determine the axial resolution of the adaptive optics scanning laser ophthalmoscope (AOSLO). The instrument is briefly described, and the imaging results from human subjects are compared with (a) the estimated axial resolution values for a diffraction-limited, double-pass instrument and (b) the measured one for a calibrated diffuse retinal model. The comparison showed that the measured axial resolution, as obtained from optical sectioning of human retinas *in vivo*, can be as low as 71 μm for a 50 μm confocal pinhole after focusing a 3.5 mm beam with a 100 mm focal-length lens. The axial resolution values typically fall between the predictions from numerical models for diffuse and specular reflectors. This suggests that the reflection from the retinal blood vessel combines diffuse and specular components. This conclusion is supported by the almost universal interpretation that the image of a cylindrical blood vessel exhibits a bright reflection along its apex that is considered specular. The enhanced axial resolution achieved through use of adaptive optics leads to an improvement in the volume resolution of almost 2 orders of magnitude when compared with a conventional scanning laser ophthalmoscope and almost a factor of 3 better than commercially available optical coherence tomographic instruments. © 2005 Optical Society of America

OCIS codes: 010.1080, 170.0110, 350.5730, 170.4470.

1. Introduction

Optical imaging of the living human retina with high-resolution instrumentation is of increased interest. It allows the diagnosis and evolution of eye pathologies¹⁻⁵ and the required monitoring after treatment. Basic anatomical questions about different microscopic features in the fundus of the eye can also be studied and characterized.⁶⁻¹¹

Furthermore, three-dimensional (3-D) images reconstructed from optical sectioning of thick specimens, like the retinal tissue in humans, are also desirable. The adaptive optics scanning laser ophthalmoscope (AOSLO) at the University of Houston, as described in a previous publication,¹² is a confocal

instrument with enhanced lateral resolution and unmatched capabilities of optical sectioning.

In this study we present the first quantitative measurement to our knowledge of the axial resolution with the AOSLO on human and model eyes. We used this instrument to collect retinal images of different retinal features and at different focal planes from three subjects. Following standard procedures in confocal microscopy¹³⁻¹⁵ we also scanned a perfect diffuse reflector (99% certified diffuse reflectance standard Spectralon¹⁶ at the retinal plane of a model eye, which corresponds to the specimen plane in a confocal microscope) through focus and noted the intensity response to determine the full width at half-maximum (FWHM) as the metric of the optical sectioning capabilities of the AOSLO. In the data processing of the image sequences, plots of measured intensity as a function of axial depth were used to directly determine the axial resolution of the instrument.

Reducing ocular aberrations in an effort to obtain axial resolution improvements in a scanning laser ophthalmoscope (SLO) has been studied previously by Dreher *et al.*¹⁷ who used an active element to remove astigmatism in a SLO and by Bartsch *et al.*¹⁸ who eliminated the aberrations of the cornea by using a contact lens on the eye. In both cases

When this research was performed, F. Romero-Borja (fromero@uh.edu), K. Venkateswaran, and A. Roorda were with the College of Optometry, University of Houston, 4800 Calhoun Road, Houston, Texas 77204-2020. A. Roorda (aroorda@berkeley.edu) is now with the School of Optometry, University of California, Berkeley, Berkeley, California 94720. T. Hebert is with the Cullen College of Engineering, University of Houston, 4800 Calhoun Road, Houston, Texas 77204-4007.

Received 15 June 2004; revised manuscript received 27 January 2005; accepted 12 February 2005.

0003-6935/05/194032-09\$15.00/0

© 2005 Optical Society of America

they reported improvements, but they were moderate because at that time neither group had the technology to reach the level of aberration correction of the AOSLO.

2. Methods

A. Instrument

The confocal scanning laser microscope^{19,20} and the confocal SLO^{21,22} are instruments based on laser scanning imaging techniques. The instruments have impressive imaging capabilities, which include real-time, high-contrast imaging with optical sectioning. It is well known that the image quality in microscopy is strongly dependent on the quality and correcting properties of the microscope objective.^{23,24} In the case of the SLO, the imaging capabilities are especially restricted by the quality of the optics in the human eye because the optics of the eye, which are fraught with aberrations, serve as the objective lens. The AOSLO utilized in this study is the merging of adaptive optics (AO) used to correct optical aberrations of the eye^{25–27} and a SLO with all its good capabilities. The six main components of the instrument are the following:

(i) Light delivery system. Light from a laser diode of a selected wavelength is coupled into the instrument by way of a single-mode optical fiber whose output end provides a point source of light. The single scanning light source is used for both imaging and wave-front sensing.

(ii) Wave-front sensing. Wave-front sensing is accomplished by a Shack–Hartmann sensor with a square lenslet array and a digital CCD camera. This allows us to fit the wave-front aberrations (produced by the eye defects and the instrument design constraints) to an eighth-order Zernike polynomial.

(iii) Wave-front compensation. A 37-channel deformable mirror (DM) conjugate to the entrance pupil of the eye is used to compensate the aberrations. After the aberrations are measured in the wave front and are fitted to the Zernike polynomial, the DM is shaped correspondingly to correct the wave front of the light on its path into the eye, as well as the wave front of the light on its return path toward the confocal pinhole at the detection (imaging) arm.

(iv) Raster scanning. A resonant and a galvanometric scanner combination is used to scan the laser beam onto the retina to illuminate a region of approximately 1.5 by 1.4 deg. The current setup allows us to collect video at a rate of 30 frames/s.

(v) Light detection. Diffusely reflected light from the focused spot on the retina is refocused onto the confocal pinhole and detected by a GaAs photomultiplier tube (PMT).

(vi) Frame grabbing. A Matrox Genesis frame grabber makes possible the digital image reconstruction from the PMT signal after some signal conditioning has taken place. An updated version of the instrument optical layout is shown in Fig. 1.

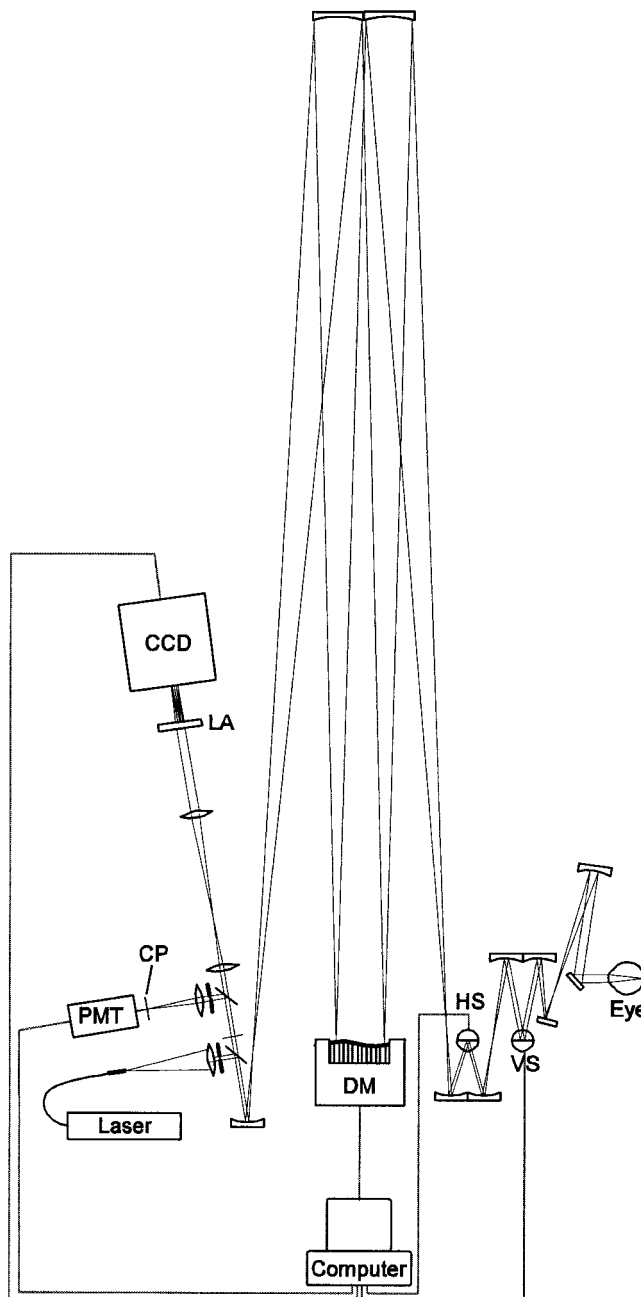


Fig. 1. Current optical layout of the AOSLO. Light from the laser is relayed to the DM, the horizontal scanner (HS), the vertical scanner (VS), and finally to the eye through a series of afocal mirror telescopes. Scattered light from the retina returns through the same path and focuses to the confocal pinhole (CP) and PMT detector. A fraction of the light is diverted to the Shack–Hartmann wave-front sensor with a lenslet array (LA) comprised of 400 μm lenslets.

B. Imaging Protocol

Three subjects participated in this study (they are noted here as AR, RS, and SB). The subjects were normal healthy males with ages from 26 to 37 years. The left eye of each subject was imaged. In preparation for each imaging session, the subject's eye was dilated and its accommodation paralyzed with mydriatic agents (tropicamide 1% and phenylephrine

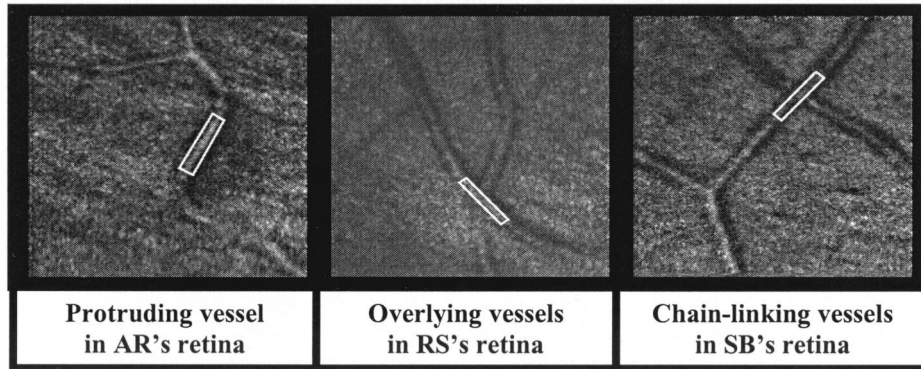


Fig. 2. Images of the microscopic features imaged *in vivo* in the retinas of the three subjects that participated in this axial resolution study with the AOSLO instrument. All three features are in the subjects left eye at ≈ 4.5 deg superior to the fovea. The region of interest (ROI) for axial scanning is shown above as a white box for each subject. The area of the ROI is on average 2400 square pixels.

2.5%, one drop of each and a repeat application after 5 min). A personalized bite bar was prepared using a customized dental impression tray and impression compound cakes. The bite bar was attached to an x, y, z translation stage to allow the subject to maintain stable eye position and alignment during the imaging session.

Videos were recorded with the AOSLO using a wavelength of 660 nm and scanning through focus, with the AO correction in closed loop mode to minimize inducing new aberrations. Five different confocal pinhole diameters were used in this study: 50, 80, 100, 150, and 200 μm in diameter. To put the pinhole sizes into context, the light at the confocal pinhole was formed by a 3.5 mm beam focused with a 100 mm focal-length lens (N.A. of 0.017). Thus the Airy disk radius at the confocal pinhole in a diffraction-limited system would be 23 μm .

After retinal exploration for each one of the subjects, a specific retinal feature was selected. These features included blood vessels and capillaries at the same eccentricity. The selected retinal feature and location was any well-defined vessel or vessel network at an eccentricity of 4–5 deg superior to the fovea. A sampler of individual frames for these subjects is shown in Fig. 2.

Once the specific feature was selected for a given subject, a fixation target was provided for that eccentricity, and the high-order aberrations were AO corrected. At this point, a video was recorded at regular time intervals as a specific amount of defocus was introduced with the DM. This procedure was repeated for each subject with five different confocal pinhole sizes: 50, 80, 100, 150, and 200 μm in diameter. The widest range of the through-focus scan was from -0.8 to $+0.8$ diopter (D), which corresponded to an axial depth range of approximately -300 to $+292$ μm . To determine this axial range, we assume the Emsley's version of the reduced eye for which in the unaccommodated eye the power is $+60$ D and the index of refraction is $4/3$. The shift of imaging plane, in micrometers, is thus given by the simple expression $(4/3) \{ [1/(60 \text{ D} + \text{defocus})] - [1/(60 \text{ D})] \} \times 10^6$.

The area imaged was determined by the retinal raster scan sweeping an angle of 1.5 by 1.4 deg. During the through-focus operation, the AO correction was active in the closed-loop mode to minimize the induction of new aberrations as the defocus was applied. This was made possible by closing the AO loop to a specified defocus aberration rather than zero aberration. This beneficial effect of a dynamic AO correction during an axial scan is shown for the model eye in Fig. 3, which shows axial through-focus intensity curves under the uncorrected condition, with a static AO correction with applied defocus and under

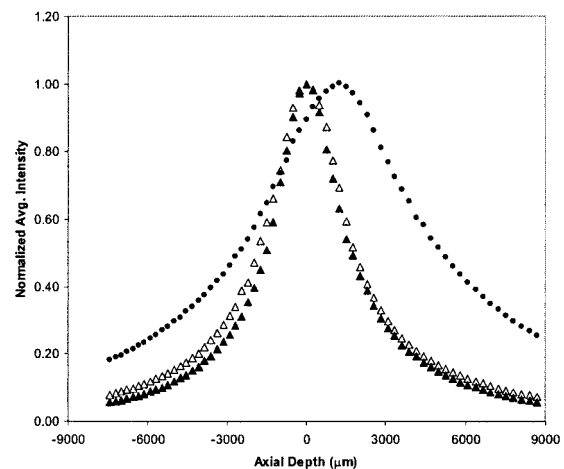


Fig. 3. Normalized axial intensity versus axial depth for the AOSLO to determine the axial resolution when operating in three different modes: closed-loop, \blacktriangle (dynamic AO correction); open-loop, \triangle (static AO correction); and as a standard SLO instrument, \bullet (no AO correction). The measured axial resolution (FWHM) for each case was 3200, 3700, and 7700 μm , respectively. The corresponding equivalent values for the reduced eye were 120, 138, 278 μm , respectively. These measurements were performed using the 10 D model eye with the 99% certified, diffuse reflectance standard and the 80 μm pinhole. The lateral shift in the uncorrected curve is due to some residual defocus that was present before AO correction.

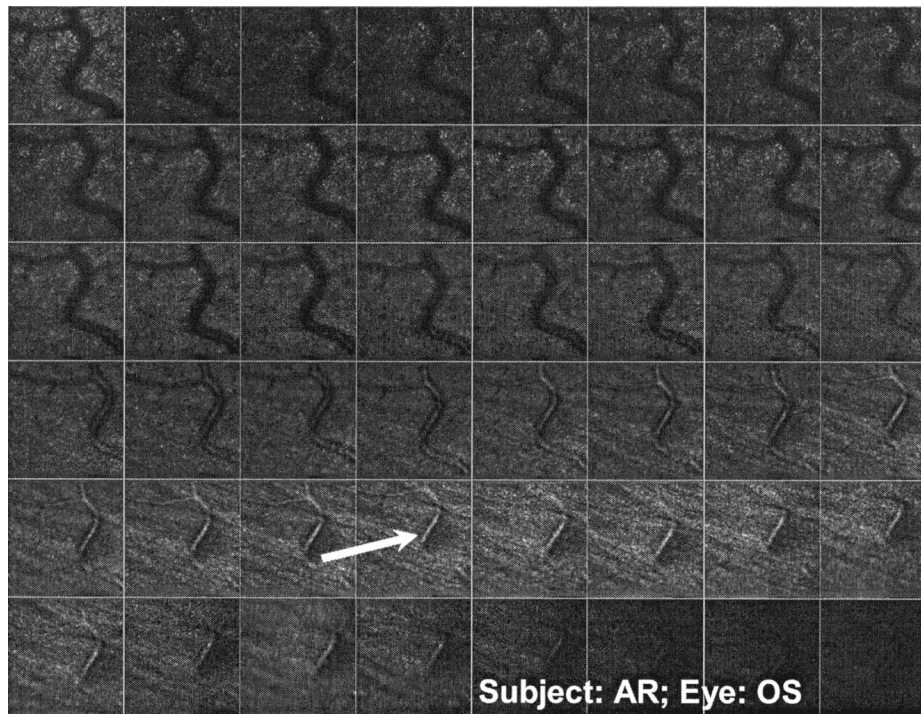


Fig. 4. Optical sections of a retinal region *in vivo* captured by the AOSLO. This composite is generated from video imaging while scanning axially through focus. This is a protruding vessel in the superior retina of AR's left eye [oculus sinister (OS)]. The scan is calibrated to move in steps of $\approx 9 \mu\text{m}$ starting at the posterior retina and moving up to the anterior retinal surface where the nerve fiber layer can be recognized. Each frame is the image of an average of ten registered frames of a $1.4 \text{ deg} \times 1.5 \text{ deg}$ region. The white arrow points to the selected feature (ROI) for which the average intensity curve as a function of axial depth was measured. It is worth mentioning that the photoreceptor layer is also resolved and recognizable in this composite along the upper rows of this image composite.

closed-loop AO correction with applied defocus. The closed-loop mode provides the smallest FWHM. The widening originates from residual aberrations and induced aberrations caused by the superimposing of a defocus onto the DM. In the human eye the improvement is expected to be even greater because, unlike the model eye, the aberrations of the human eye are not only higher, but they are dynamic and, if left uncorrected, will add new aberrations to the beam over time. Reductions in axial resolution due to the presence of aberrations have been recognized by several authors in previous axial depth studies.^{17,25,28}

C. Data Processing

The optical slicing of the selected retinal feature and surrounding tissue, as described above, yielded a sequence of images at different imaging planes as can be seen in Fig. 4. The frame shown for each axial depth in these composites is a registered and averaged set of ten frames to improve the signal-to-noise ratio. The different image planes were scanned to determine the average intensity of a small region of interest (ROI) of ≈ 2400 square pixels along the top of the retinal feature (vessel) as function of the axial depth (defocus). Selecting a blood vessel is possible thanks to the high lateral resolution of the AOSLO and because it is the best approximation to a single surface with the least obstructed view by neural tissue. The FWHMs were obtained for the curves of intensity versus axial depth measured for each of the

subjects and the corresponding retinal feature. The curves generated with the five confocal pinhole sizes mentioned above are shown in Fig. 5 for subject AR. The FWHM values as a direct measure of the axial resolution of the AOSLO at the specified wavelength are given in Table 1 for the first group of measurements in this study.

3. Results

A. Measurements *In Vivo* with Different Pinhole Sizes

For comparison with *in vivo* measurements, we use a theoretical model developed previously²⁹ in which the axial resolution of a double-pass imaging instrument was calculated for a retina that has either specular³⁰ or a diffuse reflecting surface.³¹ Axial resolution was computed from the change in detected intensity as the retinal plane was moved through the focal plane of the eye. As has been previously reported in the literature,^{14,15,17,30} the model predicts an increase in axial resolution with decreasing aberrations and for decreasing pinhole sizes. Following this concept, curves of intensity $i(u)$ versus axial depth for the different pinholes as obtained for AR are shown in Fig. 5; similar curves were obtained for the other two subjects. The solid thick curves that circumscribe the curves for the 200 and 50 μm pinholes are examples of a best curve fit after Fourier filtering, which was used to obtain a better defined FWHM since the ragged appearance of the *in vivo* experimental curves

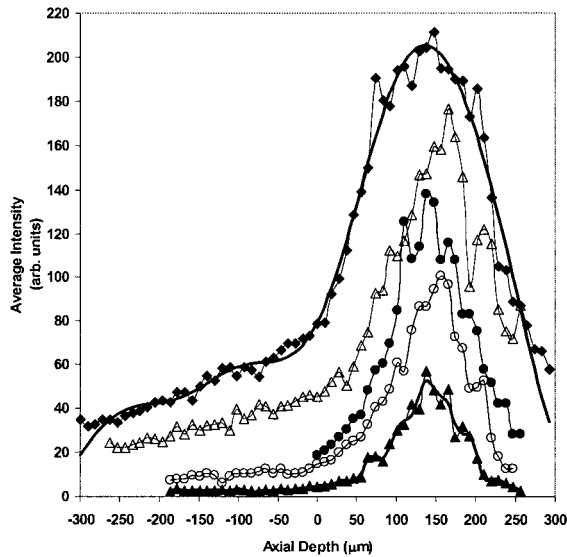


Fig. 5. Average intensity versus axial depth for a human retina *in vivo* to determine the axial resolution of the AOSLO in direct clinical applications. These curves were generated for five different pinhole sizes from image composites of video frames digitally recorded with the AOSLO. The symbols \blacklozenge , \blacktriangle , \bullet , \square , and \blacktriangleup represent pinhole sizes of 200, 150, 100, 80, and 50 μm , respectively. The solid thick curves circumscribing the 200 and 50 μm curves are examples of the curve fit after the Fourier filtering of the raw data. A typical composite of the through-focus scan is shown in Fig. 4 for one of the subjects, and the experimental axial resolution values for all three subjects in this part of the study are listed in Table 1.

make hard (sometimes) the determination of the axial resolution. Similar envelopes were determined for all pinholes and all three subjects.

The Fourier low-pass filtering, used to smooth out the raw data, is based on the following assumption. From theory we know that the presence of aberrations makes the axial intensity profile broader, hence

Table 1. FWHM Values for Similar Curves as Those Shown in Fig. 5 for the Three Human Retinas^a

Pinhole Size (μm)	FWHM (μm) (Raw Average Intensity Curve)			FWHM (μm) (Fourier-Filtered Data)		
	AR	RS	SB	AR	RS	SB
50	94	142	66	98	147	71
80	119	173	120	110	204	120
100	114	243	104	112	293	123
150	158	214	162	171	223	154
200	195	279	196	221	330	209

^aFor all subjects a ROI of 2400 square pixels on the top of a distinct retinal vessel at an eccentricity of ≈ 4.5 deg superior of the left eye was selected for axial scanning. Some of the obtained curves were noisier than others depending on the subject's ability to keep fixation and tear breakup characteristics and whether the imaging session ran smoothly or under stressful conditions. We decided, for consistency, to fit curves to all our *in vivo* raw data by Fourier filtering in this part of the experiment and presented it along with the raw data.

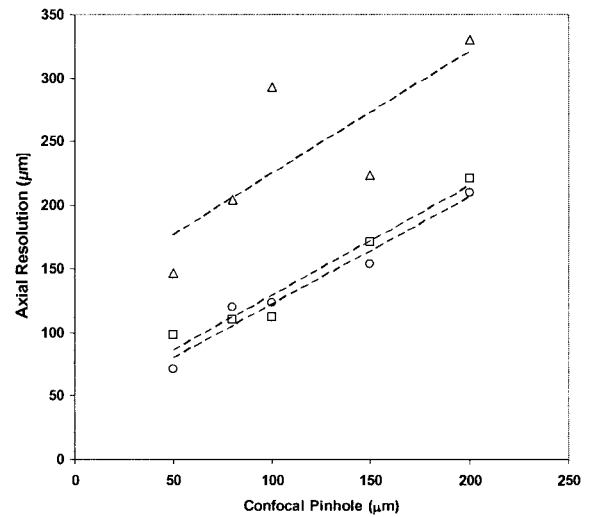


Fig. 6. Axial resolution for the AOSLO as measured from three human retinas *in vivo*. Plotted are values from best fits to the experimental curves after the Fourier filtering of the raw data, as explained in the caption of Table 1. The straight lines are linear fits showing the trend that the data values follow for each of the three subjects. The symbols \square , \triangle , and \circ represent data points for AR, RS, and SB, respectively.

the axial intensity profiles of human subjects are broader than the axial intensity profile of the model. The process is as follows. The Fourier transform of $i(u)\{I(U) = FT[i(u)]\}$ is multiplied by a low-pass filter:

$$W(U) = \begin{cases} 1 & \text{for } 0 \leq U \leq f_c \\ 0 & U > f_c \end{cases}, \quad (1)$$

where f_c is the cutoff frequency of the filter. The low-pass-filtered axial intensity profile is then

$$i_L(u) = FT^{-1}[I(U)W(0 \leq U \leq f_c)]. \quad (2)$$

Appropriate cutoff frequencies were determined from axial intensity curves from an artificial eye, which were much smoother than the human eye data. The lowest value of f_c for which the FWHM of the filtered data matched the FWHM from the raw data of the artificial eye was used as the f_c in the low-pass filter for the noisy axial intensity profiles of the human eye. The low-pass-filtered axial intensity profiles give smoother axial intensity profiles and more realistic estimates of the axial resolution.

The values of the axial resolution determined from the raw data and from the curve fits after Fourier filtering for the different subjects and pinhole sizes are summarized in Table 1. From this point on, only the FWHM values based on the filtered data will be reported. Figure 6 shows a plot of the axial resolution as a function of the confocal pinhole size for the three subjects in the study.

B. Model Eye with Calibrated Diffuse Retina

To support and strengthen our analysis of the *in vivo* measurements of the axial resolution for the AOSLO,

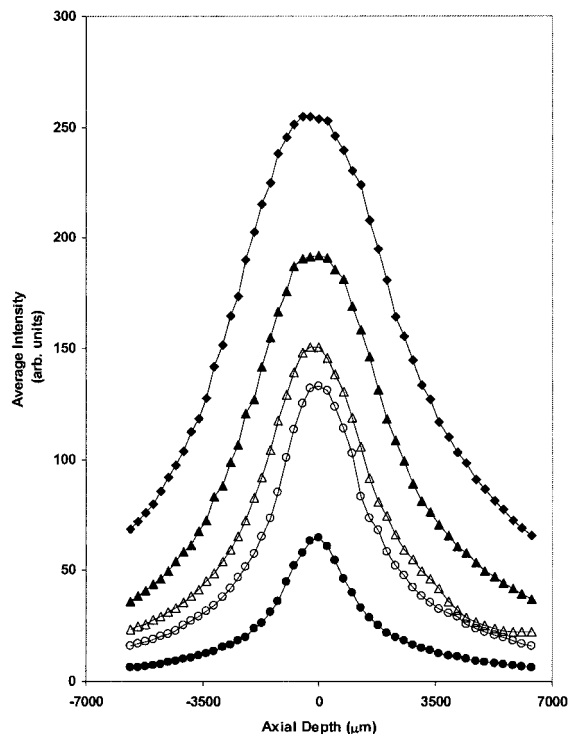


Fig. 7. Curves of average axial intensity versus axial depth for a model eye in which the retinal plane is occupied by a calibrated diffuse reflectance standard (Spectralon with 99% diffuse reflectance in the visible range) and where the cornea and crystalline lens are mimicked by a 10 D achromat lens. The symbols \blacklozenge , \blacktriangle , \circ , \triangle , and \bullet represent data points for the 200, 150, 100, 80, and 50 μm pinholes, respectively. The experimental axial resolution values (FWHM of these curves) for the five different pinhole sizes are listed in Table 2.

we measured a model eye in which the retina is a certified calibrated standard (Spectralon by Labsphere) with 99% diffuse reflectance. The eye model used a 10 D achromat lens to mimic the refracting elements of the eye. The intensity versus axial depth curves experimentally obtained for this model eye (using five confocal pinhole sizes similar to those used in the *in vivo* measurements and the same defocus range from -0.8 to $+0.8$) are shown in Fig. 7.

Even though this is not a perfect phantom of a human eye, these measurements can be used easily to gauge the equivalent axial resolution of the human eye. First, it is important to note that the raw data always tabulate the change in intensity versus the defocus in diopters from the corrected state. To compute the actual axial resolution for the model eye, we compute how a change in defocus causes a shift in the image plane by taking the inverse of the lens power plus defocus. To convert a change in defocus to an equivalent axial displacement for a reduced eye, we simply have to consider the same defocus values added to a 60 D lens in a medium with an index of refraction of $4/3$. This conversion yields an estimate of the instrument's axial resolution for the reduced eye (equivalent to the Gullstrand eye model for the N.A. of the AOSLO entrance beam). The correspond-

Table 2. Axial Resolution Values for the 10 D Eye (Model Eye with Spectralon Retina) for Raw Experimental FWHM Values^a

Pinhole Size	FWHM 10 D Eye; $n = 1$	Equivalent FWHM 60 D Eye; $n = 4/3$
50	2700	101
80	3450	130
100	4100	154
150	5350	200
200	6700	250

^aThe third column lists equivalent values for a reduced eye model (60 D eye with index of refraction $n = 4/3$). The linear relationship between the axial resolution and the size of the confocal pinhole calculated from the reduced eye data is displayed in Fig. 8.

ing axial resolution values for the five different pinhole sizes are listed in Table 2 and could be used as a reference when the axial measurements are performed *in vivo*.

Finally, in Fig. 8 we also plotted the axial resolution data of the reduced eye as a function of the pinhole size and fitted a straight line to it, which allowed us to give an expression of the functional dependence between the axial resolution values for different pinhole sizes in the case of our reduced eye model.

4. Discussion

Measuring the resolution of any imaging instrument is an important component of an instrument's characterization and an indicator of its strengths. For the AOSLO, axial resolution is one of the most important performance metrics. Not only does axial resolution

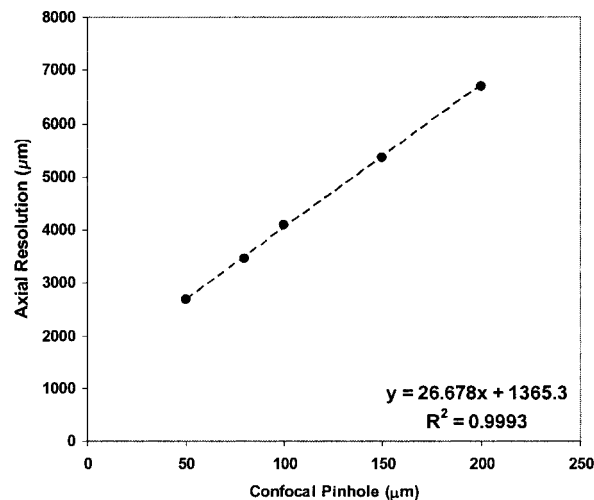


Fig. 8. Axial resolution as a function of the confocal pinhole size for the reduced eye. The data points plotted here were calculated from experimental measurements of a model eye with a certified diffuse reflectance standard at the retinal plane. FWHM data from the second column in Table 2 are plotted here as functions of the confocal pinhole size in micrometers. The straight line fitted to the data yielded the functional dependence to calculate the axial resolution for this reduced eye model.

indicate the ability of the AOSLO to do true optical sectioning of retinal tissue, but it also serves to increase the contrast of any retinal layer that is being imaged. This is important as we attempt to visualize low-contrast features in the retina, for example, the ganglion cells. The instrument is designed to image the retina *in vivo*, which is a complex structure with diffuse reflecting properties. A simplistic approach to measure the axial resolution of the instrument would be to use a diffuse or specular reflector (as is customarily done with the standard confocal microscopes) at the plane where the retina (specimen) is usually located. The axial resolution obtained in that way could be considered a nominal axial resolution but it would not be, however, a realistic one for practical applications like optical sectioning or 3-D reconstruction of retinal structures. This is because the optics of the eye (playing the role of the objective lens in the ophthalmoscope) is different for the different subjects or patients. Furthermore, the residual aberrations for each individual will be different because AO systems are not perfect. This led us to incorporate in our study different eyes and different retinal features with the intention of obtaining more realistic figures for the axial resolution of the instrument.

The axial resolution of a standard SLO is generally in the range of 300 μm .^{15,32} All the experimental figures obtained here for the axial resolution of the AOSLO, with the frequently used 80 μm pinhole, are in the range from 204 μm (for the noisiest measurement) to 110 μm , which are, in either case, well below the 300 μm mark just mentioned for the standard SLO instrument. Furthermore, we report axial resolutions as low as 71 μm for smaller confocal pinholes. The only axial resolution measurements that approached the 300 μm mark were from subject RS. RS's poor axial resolution represents a significant discrepancy compared with the other two subjects in the study. The imaging session for RS became a very long one that extended over several hours causing some fatigue for the subject and affecting his ability to fixate properly. The subject is, furthermore, known to have tear film with a very short breakup time yielding to a sudden decrease in the intensity and the corresponding variations in the image quality,^{33,34} especially when the eye is forced to fixate over extended periods of time. Therefore the likely explanation for the poorer results is increased amounts of unmeasured aberrations (high-order aberrations from the tear film) and higher residual aberrations after AO correction (due to the fact that the optical system was unstable and the AO system did not have the bandwidth to keep up with the changes). The noticeable differences for RS in Fig. 6 and in Fig. 9 should, therefore, be understood only as an indicator of how strongly this *in vivo* measurement depends on the subject, and not as an error in the measurements or a factual degradation of the resolution of the instrument.

Notwithstanding the potential noisy character of the *in vivo* measurements, when we compare Fig. 6 for the human retina *in vivo* (AR and SB) and Fig. 8

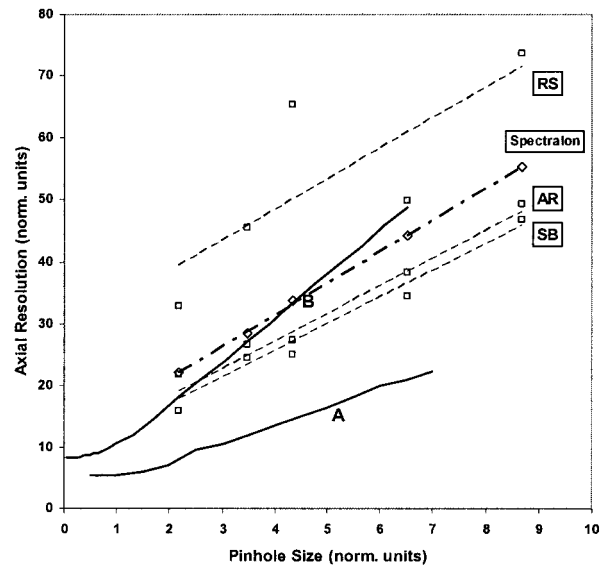


Fig. 9. Theoretically computed axial resolution for (A) a plane specular reflector and (B) a diffuse reflector. Measurements for the human eye *in vivo* were performed using five different confocal pinhole sizes: 50, 80, 100, 150, and 200 μm . The open squares (\square) represent the raw axial resolution (FWHM) values experimentally measured on the three subjects AR, RS, and SB. These are listed in Table 1. The dashed lines are best straight-line fits to indicate the trend of the axial resolution for each subject. The experimental data points for the diffuse reflector Spectralon were obtained using confocal pinholes in the range of 30–200 μm .

for the static Spectralon reduced eye, we notice that both are similar. This is true not only for the good fit to the straight line, but also for the actual value of the axial resolution in both cases. If we extract numbers from the linear best-fitting equation for an 80 μm pinhole, then the reduced eye yields an axial resolution of 131 μm and the human eyes yield 111 and 105 μm for AR and SB, respectively. These axial resolution values for the *in vivo* measurements are lower than the 120 μm mark for the theoretical model of the diffraction-limited instrument for a purely diffuse reflector.²⁸ The narrow FWHM measured for the living human retinas indicate, in our opinion, that the signal getting to the detector might contain a specular component in it, for which the axial resolution is expected to be better than the diffraction-limited one predicted for the purely diffuse reflector. Figure 9 displays the theoretical models for the axial resolution as a function of the pinhole size for a purely diffuse reflector and for a plane specular reflector; these are shown along with the raw data of the *in vivo* measurements and experimental data points for the reduced eye model with a diffuse reflector (99% certified diffuse reflectance standard Spectralon) at the retinal plane. This plot uses normalized units in both axes as in Wilson's early studies.^{13,30} The convenient dimensionless pair of (u, v) coordinates, which allows results from all model eyes and real eyes to be put on a common scale, are defined as follows:

Table 3. Parameters Used in the Conversion to the Optical, Dimensionless Coordinates u and v ^a

Parameter	Human Eye ^a	Model Eye ^b
Beam radius (in mm)	2.945	2.945
Wavelength (in μm)	0.660	0.660
Focal length (in mm)	16.667	100
Numerical aperture	0.177	0.029
Airy disk radius at the retina (μm)	1.15	6.92
Airy disk radius at the confocal pinhole (μm)	11.50	11.50
Magnification (disk at pinhole/disk at retina)	9.973	1.663
Index of refraction	1.333	1

^aData represent the 60 D reduced eye.

^bData refer to the Spectralon phantom eye with the 10 D achromat lens.

$$u = (8\pi n/\lambda)z \sin^2(\alpha/2), \quad (3)$$

$$v = (2\pi/\lambda)(d/Mv_A)\sin(\alpha), \quad (4)$$

where the axial coordinate u is directly related to the real axial distance z (e.g., the FWHM in micrometers) and the normalized, radial coordinate v is directly related to the pinhole diameter d in the object plane; λ is the imaging wavelength; $n \sin(\alpha)$ is the N.A. of the eye and eye model; n is its index of refraction; α is the one-half angular aperture of the objective, i.e., the eye itself in the case of the ophthalmoscope; v_A is the dimensionless Airy disk diameter; and M is the magnification between the object and the detector (pinhole plane). Some of these parameters used in the preparation of Fig. 9 are listed in Table 3.

A careful analysis of these plots and the experimental data seem to indicate that the reflectors considered in the study, including the human retina, are neither pure diffuse reflectors nor pure specular reflectors. This kind of behavior has been observed in previous studies³⁵ where different retinal surfaces and eye movements are responsible for influencing the accuracy and purity of the detected signal.

Figure 9 also shows that the axial resolution measured from the model eye with the diffuse reflection standard does not match closely with the theoretical predictions for a model eye (curve B). An investigation of the axial reflections from different surfaces is currently ongoing in another study.

In summary, the axial resolution values from the *in*

vivo measurements (AR and SB) were as low as 71 and 209 μm for confocal pinholes of 50 and 200 μm . These values lie between those predicted by the models for the diffuse and specular reflector, which, for the same 50 and 200 μm pinhole sizes, were 83 and 286 μm and 36 and 121 μm , respectively. The axial resolution measured from the diffuse, artificial eye model (Spectralon retina) was also within that range, even though it was in closer agreement with the diffuse theoretical model.

Finally, the 3-D resolution element (V_{resel}), which is defined as a cylinder in object space (diameter equal to the lateral resolution and length equal to the axial resolution) of the imaging instrument, is substantially improved with the improved resolution of the AOSLO. Considering that the lateral resolution of the AOSLO benefits also from the AO correction and can be as small as 2.5 μm (Refs. 12 and 36) along with our best measurement here of 71 μm for the axial resolution, the resolution element V_{resel} is equal to 340.8 μm^3 . This value is compared in Table 4 with the conventional SLO¹⁵ and with commercially available optical coherence tomography (OCT) instruments that have superb axial sectioning ability but poor lateral resolution.

5. Conclusion

The AOSLO has a greater than three times improvement in axial resolution over conventional instruments. Combined with its lateral resolution, the overall 3-D resolution approaches 2 orders of magnitude improvement over conventional SLOs. Axial resolution was shown to improve with decreasing pinhole size and, for the smallest pinholes, was as low as 71 μm . The improved resolution is gained through use of AO, which reduces the blur caused by aberrations.

The axial resolution reported here facilitates true optical sectioning of the layers in the retina, which ranges in thickness from 200 to 300 μm . Furthermore, the improved axial resolution will increase the contrast of all resolved features in the focal plane. Improved axial resolution represents an important advance in the effort to provide noninvasive microscopic imaging of retinal tissue in normal and diseased eyes.

This research was funded by a National Institutes of Health and National Eye Institute grant EY13299-01 to A. Roorda and also by the National Science Foundation Science and Technology Center

Table 4. Comparison of the 3-D Resolution Element for the AOSLO, the Conventional SLO, and the Low-Coherence Technique OCT^a

Instrument	Lateral Resolution (μm)	Axial Resolution (μm)	V_{resel} (μm^3)	Compared with AOSLO
AOSLO	2.5	71	348	1
Conventional SLO	5–10	300	5890–23,562	17–68 times worse
Conventional OCT	10–20	10	785–1571	2.2–4.5 times worse

^aThe values for a commercial SLO are typical amounts inferred from the literature. OCT values are taken from the Stratus OCT product information (Carl Zeiss Meditec, Dublin, California). Transverse resolution is reported as high as 20 μm because OCT instruments are generally limited by the size of the pixel (sampling resolution), not by optical resolution.

References

1. M. A. Mainster, G. T. Timberlake, R. H. Webb, and G. W. Hughes, "Scanning laser ophthalmoscopy. Clinical applications," *Ophthalmology* **89**, 852–857 (1982).
2. F. Koenig, G. Timberlake, A. Jalkh, C. Trempe, F. van de Velde, and G. Coscas, "Scanning laser ophthalmoscopy. Its value in macular diseases," *J. Fr. Ophthalmol.* **13**, 253–258 (1990).
3. D. U. Bartsch, M. Intaglietta, J. F. Bille, A. W. Dreher, M. Gharib, and W. R. Freeman, "Confocal laser tomographic analysis of the retina in eyes with macular hole formation and other focal macular diseases," *Am. J. Ophthalmol.* **108**, 277–287 (1989).
4. W. N. Wykes, A. A. Pyott, and V. G. Ferguson, "Detection of diabetic retinopathy by scanning laser ophthalmoscopy," *Eye* **8**, 437–439 (1994).
5. S. Asrani, R. Zeimer, M. F. Goldberg, and S. Zou, "Serial optical sectioning of macular holes at different stages of development," *Ophthalmology* **105**, 66–77 (1998).
6. D. van Norren and J. van de Kraats, "Imaging retinal densitometry with a confocal scanning laser ophthalmoscope," *Vision Res.* **29**, 1825–1830 (1989).
7. F. W. Fitzke and B. R. Masters, "Three-dimensional visualization of confocal sections of *in vivo* human fundus and optic nerve," *Curr. Eye Res.* **12**, 1015–1018 (1993).
8. F. W. Fitzke, "Imaging the optic nerve and ganglion cell layer," *Eye* **14**, 450–453 (2000).
9. D. M. Foreman, S. Bagley, J. Moore, G. W. Ireland, D. McLeod, and M. E. Boulton, "Three dimensional analysis of the retinal vasculature using immunofluorescent staining and confocal laser scanning microscopy," *Br. J. Ophthalmol.* **80**, 246–251 (1996).
10. R. Birngruber, U. Schmidt-Erfurth, S. Teschner, and J. Noack, "Confocal laser scanning fluorescence topography: a new method for three-dimensional functional imaging of vascular structures," *Graefes Arch. Clin. Exp. Ophthalmol.* **238**, 559–565 (2000).
11. S. G. Rosolen, G. Saint-MacAry, V. Gautier, and J. F. Legargasson, "Ocular fundus images with confocal scanning laser ophthalmoscopy in the dog, monkey and minipig," *Vet. Ophthalmol.* **4**, 41–45 (2001).
12. A. Roorda, F. Romero-Borja, W. J. Donnelly, H. Queener, T. J. Hebert, and M. C. W. Campbell, "Adaptive optics scanning laser ophthalmoscopy," *Opt. Express* **10**, 405–412 (2002).
13. T. Wilson, *Confocal Microscopy* (Academic, 1990).
14. T. R. Corle and G. S. Kino, "Depth and transverse resolution," in *Confocal Scanning Optical Microscopy and Related Imaging Systems* (Academic, 1996).
15. G. Gaida, "Perspectives and limits of three dimensional fundus microscopy," in *Scanning Laser Ophthalmoscopy and Tomography*, J. E. Nasemann and R. O. W. Burk, eds. (Quintessenz, 1990).
16. Spectralon reflectance material is a perfectly diffuse reflecting material that is ideal for applications ranging from the UV-visible to the near-infrared to mid-infrared wavelength region. Spectralon is a highly Lambertian, thermoplastic material that can be machined into a wide variety of shapes to suit any reflectance component requirement. Spectralon is a registered product marketed by Labsphere, Inc. North Sutton, N.H.
17. A. W. Dreher, J. F. Bille, and R. N. Weinreb, "Active optical depth resolution improvement of the laser tomographic scanner," *Appl. Opt.* **28**, 804–808 (1989).
18. D. Bartsch, G. Zinser, and W. R. Freeman, "Resolution improvement in confocal scanning laser tomography of the human fundus," *Vision Science and its Applications*, Vol. 2 of OSA Technical Digest Series (Optical Society of America, 1994), pp. 134–137.
19. T. Wilson and C. J. R. Sheppard, *Theory and Practice of Scanning Optical Microscopy* (Academic, 1984).
20. C. J. R. Sheppard, "Scanning optical microscopy," in *Advances in Optical and Electron Microscopy*, R. Barer and V. E. Coslett, eds. (Academic, 1987).
21. R. H. Webb and G. W. Hughes, "Scanning laser ophthalmoscope," *IEEE Trans. Biomed. Eng.* **28**, 488–492 (1981).
22. R. H. Webb, G. W. Hughes, and F. C. Delori, "Confocal scanning laser ophthalmoscope," *Appl. Opt.* **26**, 1492–1499 (1987).
23. H. E. Keller, "Objective lenses for confocal microscopy," in *Handbook of Biological Confocal Microscopy*, J. B. Pawley, ed. (Plenum, 1995).
24. C. J. Cogswell and K. G. Larkin, "The specimen illumination path and its effect on image quality," in *Handbook of Biological Confocal Microscopy*, J. B. Pawley, ed. (Plenum, 1995).
25. J. F. Bille, B. Grimm, J. Liang, and K. Muller, "Active-optical improvement of the spatial resolution of the laser tomographic scanner," in *Scanning Laser Ophthalmoscopy and Tomography*, J. E. Nasemann and R. O. W. Burk, eds. (Quintessenz, 1990).
26. J. Liang and D. R. Williams, "Aberrations and retinal image quality of the normal human eye," *J. Opt. Soc. Am. A* **14**, 2873–2883 (1997).
27. J. Liang, D. R. Williams, and D. Miller, "Supernormal vision and high-resolution retinal imaging through adaptive optics," *J. Opt. Soc. Am. A* **14**, 2884–2892 (1997).
28. T. Wilson and A. R. Carlini, "The effect of aberrations on the axial response of confocal imaging systems," *J. Microsc.* **154**, 243–256 (1989).
29. K. Venkateswaran, A. Roorda, and F. Romero-Borja, "Theoretical modeling and evaluation of the axial resolution of the adaptive optics scanning laser ophthalmoscope," *J. Biomed. Opt.* **9**, 132–138 (2004).
30. T. Wilson, "The role of the pinhole in confocal imaging system," in *Handbook of Biological Confocal Microscopy*, J. B. Pawley, ed. (Plenum, 1995).
31. P. Artal, I. Iglesias, and N. Lopez-Gill, "Double-pass measurements of the retinal-image quality with unequal entrance and exit pupil sizes and the reversibility of the eye's optical system," *J. Opt. Soc. Am. A* **12**, 2358–2366 (1995).
32. Heidelberg Engineering GmbH, Technical Data for the HRT and HRT-II on-line (Heidelberg Engineering GmbH, Heidelberg, Germany, 2003), www.heidelbergengineering.com/hrt2/.
33. R. Tutt, A. Bradley, C. Begley, and L. N. Thibos, "Optical and visual impact of tear break-up in human eyes," *Invest. Ophthalmol. Vis. Sci.* **41**, 4117–4123 (2000).
34. N. L. Himebaugh, A. R. Wright, A. Bradley, C. G. Begley, and L. N. Thibos, "Use of retroillumination to visualize optical aberrations caused by tear film break-up," *Optom. Vis. Sci.* **80**, 69–78 (2003).
35. D. U. Bartsch and W. R. Freeman, "Laser-tissue interaction and artifacts in confocal scanning laser ophthalmoscopy and tomography," *Neurosci. Biobehav. Rev.* **17**, 459–467 (1993).
36. W. J. Donnelly, "Improving imaging in the confocal scanning laser ophthalmoscope," Master's thesis (University of Houston, Houston, Tex., 2001).